



Provided by the author(s) and University of Galway in accordance with publisher policies. Please cite the published version when available.

Title	Design and performance of a small-animal imaging system using synthetic collimation.
Author(s)	Havelin, R. J.; Foley, Mark J.
Publication Date	2013-02-28
Publication Information	Havelin RJ, Miller BW, Barrett HH, Furenlid LR, Murphy JM, Dwyer RM, Foley MJ (2013) 'Design and performance of a small-animal imaging system using synthetic collimation'. <i>Physics In Medicine And Biology</i> , 58 (10):3397-3412.
Publisher	Institute of Physics
Link to publisher's version	http://dx.doi.org/10.1088/0031-9155/58/10/3397
Item record	http://hdl.handle.net/10379/4181
DOI	http://dx.doi.org/10.1088/0031-9155/58/10/3397

Downloaded 2024-04-26T03:04:07Z

Some rights reserved. For more information, please see the item record link above.



Design and performance of a small animal imaging system using synthetic collimation

R J Havelin¹, B W Miller², H H Barrett², L R Furenlid², M J Foley¹

¹School of Physics, National University of Ireland Galway, Ireland.

²Center for Gamma-ray Imaging, University of Arizona, Tucson, AZ, USA

E-mail: mark.foley@nuigalway.ie

Abstract. This work outlines the design and construction of a single-photon emission computed tomography (SPECT) imaging system based on the concept of synthetic collimation. A focused multi-pinhole collimator is constructed using rapid-prototyping and casting techniques. The collimator projects the centre of the field-of-view (FOV) through forty-six pinholes when the detector is adjacent to the collimator, with the number reducing towards the edge of the FOV. The detector is then moved further from the collimator to increase the magnification of the system. The object distance remains constant, and each new detector distance is a new system configuration. The level of overlap of the pinhole projections increases as the system magnification increases, but the number of projections subtended by the detector is reduced. There is no rotation in the system; a single tomographic angle is used in each system configuration. Image reconstruction is performed using maximum-likelihood expectation-maximization (MLEM), and an experimentally measured system matrix. The system matrix is measured for each configuration on a coarse grid, using a point source. The pinholes are individually identified and tracked, and a Gaussian fit is made to each projection. The coefficients of these fits are used to interpolate the system matrix. The system is validated experimentally with a hot-rod phantom. The Fourier crosstalk matrix is also measured to provide a measure of the average spatial resolution along each axis over the entire FOV. The 3D synthetic-collimator image is formed by estimating the activity distribution within the FOV, and summing the activities in the voxels along the axis perpendicular to collimator face.

Submitted to: *Phys. Med. Biol.*

1. Introduction

Single-photon emission computed tomography (SPECT) is a useful tool for small animal molecular imaging (Meikle et al. 2005). The objective of molecular imaging is to image proteins, genes, or the biochemical and molecular pathways they are involved in, within living subjects (Cherry 2004). SPECT has been used to investigate the targeting of radioisotope-labelled mesenchymal stem cells to specific locations, while also investigating engraftment capabilities (Dwyer et al. 2011). Most SPECT systems use a collimator for image formation. Common examples include parallel-hole collimators and pinhole collimators, the merits of which have been well studied (Jaszczak et al. 1994, Barrett & Swindell 1981). The collimator increases the spatial information of the photons by reducing the possible emission locations of each detected photon. Single-pinhole imaging is often plagued by relatively poor geometric efficiency, and one method for increasing the sensitivity is to use multi-pinhole collimators (Barrett & Swindell 1981).

A multi-pinhole collimator has an array of pinholes which allow the object to be imaged by different detectors or different elements of the same detector. Overlap of these pinhole projections (multiplexing) can lead to a loss of spatial information because a photon detected in this region could have passed through one of several pinholes (Mahmood et al. 2010). There is much interest in using statistical iterative algorithms to demultiplex this data to minimize the loss of spatial resolution, while increasing the active detector area (Peterson et al. 2009). The system described in this work uses the technique known as synthetic collimation which combines multiplexed and non-multiplexed data to produce high-resolution, artefact-free reconstructions (Wilson et al. 2000). By combining images of an object at different magnification factors it has been shown in simulations that the effect of multiplexing can be removed (Mahmood et al. 2010). The data contain information on how the projections overlap which enables us to reconstruct the object using maximum-likelihood estimation (Wilson et al. 2000).

This paper outlines the design and construction of a focused multi-pinhole collimator, the calibration of the system by experimental measurement of the system matrix, the interpolation of this system matrix, and the validation of the algorithm through reconstruction of a hot-rod phantom. The 3D synthetic-collimator image is formed by estimating the activity distribution within the FOV, and summing the activities in the voxels along the axis perpendicular to collimator face (Wilson et al. 2000). In this work z is defined as direction perpendicular to the collimator face.

2. Methods

The SyntheticSPECT system consists of a BazookaSPECT gamma-ray detector (Miller et al. 2006) coupled to a fiber-optic taper (Miller, Barber, Barrett, Liu, Nagarkar & Furenlid 2012). The BazookaSPECT detector consists of a Lanex[®] scintillator, image

intensifier, optical lens, and fast-frame-rate CCD camera. Data are transferred to the processing computer via a firewire interface, and the use of graphics processing units (GPUs) enables image processing in real time. The BazookaSPECT detectors use a CCD sensor to achieve high resolution and large space-bandwidth products. This sensor is operated at a high frame rate, or short exposure time, so that the optical photons associated with each gamma-ray interaction do not overlap. Each photon interaction appears as a signal spread over a small pixel region, which is called a cluster. This pixel data is used to estimate the gamma-ray interaction location (see section 2.2).

BazookaSPECT detectors use a micro-channel plate (MCP) image intensifier to provide up-front optical gain. This amplification minimizes the effect of light loss from imaging the intensifier output screen onto the CCD sensor. Incident photoelectrons from the photocathode strike channel walls of the MCP to produce secondary electrons, eventually leading to an electron cascade. The amplified charge is converted to optical photons using a phosphor screen deposited on the output window of the image intensifier. A fiber-optic taper, with a 10 cm diameter entrance face and 2.5 cm diameter exit face, is inserted between the scintillator and intensifier to increase the active area of the detector (Miller, Barber, Barrett, Liu, Nagarkar & Furenlid 2012). The output window of the dual-MCP is demagnified eight times and is imaged by the CCD camera.

Image multiplexing is the overlapping on the detector of different pinhole projections. This overlap allows for more efficient use of the detector surface so that more pinholes can be included in the collimator, thus increasing the sensitivity. However, regions of overlapping projections cannot be related to one particular aperture, and this ambiguity leads to reduced spatial resolution, and artefacts, in the tomographic reconstruction (Shokouhi et al. 2009, Mahmood et al. 2010). It has been proposed that combining data with multiple magnification factors could remove this effect as this data would contain information on how the projections are multiplexed (Wilson et al. 2000). This concept is implemented to achieve high-resolution reconstructions while maximizing the detector coverage. The system is designed so that when the collimator is placed adjacent to the detector surface there is no multiplexing at the centre of the field-of-view (FOV), and a small amount at the edge. The object-to-pinhole (OP) distance remains constant, and projection images are acquired when the detector is at six distances behind the collimator. The amount of multiplexing varies with the magnification of the system.

2.1. Multi-pinhole collimator

The multi-pinhole collimator, made of a tungsten epoxy with a density of 12 g/cm^{-3} , was constructed using rapid-prototyping and casting methods (Miller et al. 2011). The double-knife-edge (DKE) pinholes were positioned in a pseudo-random pattern at the centre of the collimator, with inter-pinhole distances of 9 mm. Multi-pinhole apertures should not be arranged in a symmetrical pattern due to artefacts in the resulting reconstructions (Vunckx et al. 2008). The pinholes were 1.0 mm in diameter, and

they were focused towards a common FOV. The FOV was chosen to be 25.4 mm at a distance of 23 mm from the central pinhole. This distance was chosen to maximize sensitivity, and ensure complete separation of pinhole apertures. The focused pinholes at the edge of the collimator would impinge on the geometry of the other pinholes if the centre of the FOV was placed closer to the collimator. This configuration results in minimal pinhole projection overlap when the pinhole-to-detector (PD) distance is at a minimum, which is set by mechanical constraints. The opening angles were calculated by projecting a collapsing cone from a central slice which is orthogonal to a line joining the centre of the FOV and the pinhole location (figure 1). One needs to find the location

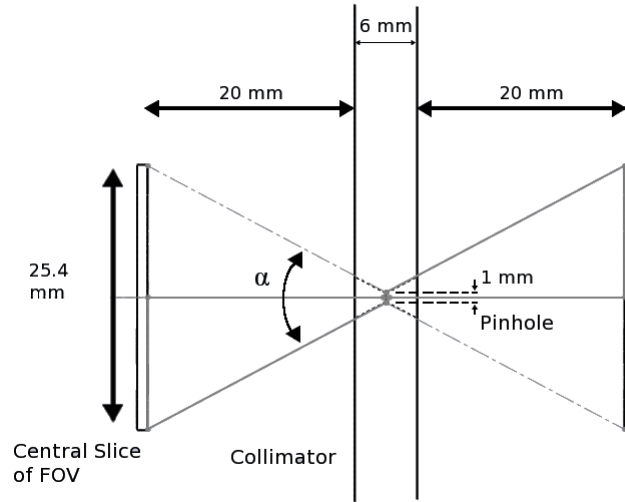


Figure 1: The pinhole geometry of the central pinhole. The opening angle, α , is calculated for each pinhole depending on its location with respect to the central point of the FOV.

of the apex of the cone which results in a pinhole of the required diameter at the centre of the collimator. From equation 1 it is easy to see that

$$\tan\left(\frac{\alpha}{2}\right) = \frac{r_1 - r_p}{d} = \frac{r_1}{d + x}, \quad (1)$$

where r_1 is the radius of the slice through the FOV, r_p is the radius of the pinhole, d is the distance between the centre of the FOV and the pinhole, and x is the orthogonal distance the apex of the cone lies behind the pinhole. Rearranging equation 1:

$$x = \frac{dr_p}{r_1 - r_p}. \quad (2)$$

Using this value for x , and the corresponding value for α , the conical geometry may be input to SolidWorksTM to create one edge of the DKE pinhole. The other edge of the pinhole is constructed in a similar manner, but its origin is a distance d behind the pinhole, along the line connecting the centre of the FOV and the pinhole coordinate. These calculations were repeated for every pinhole location.

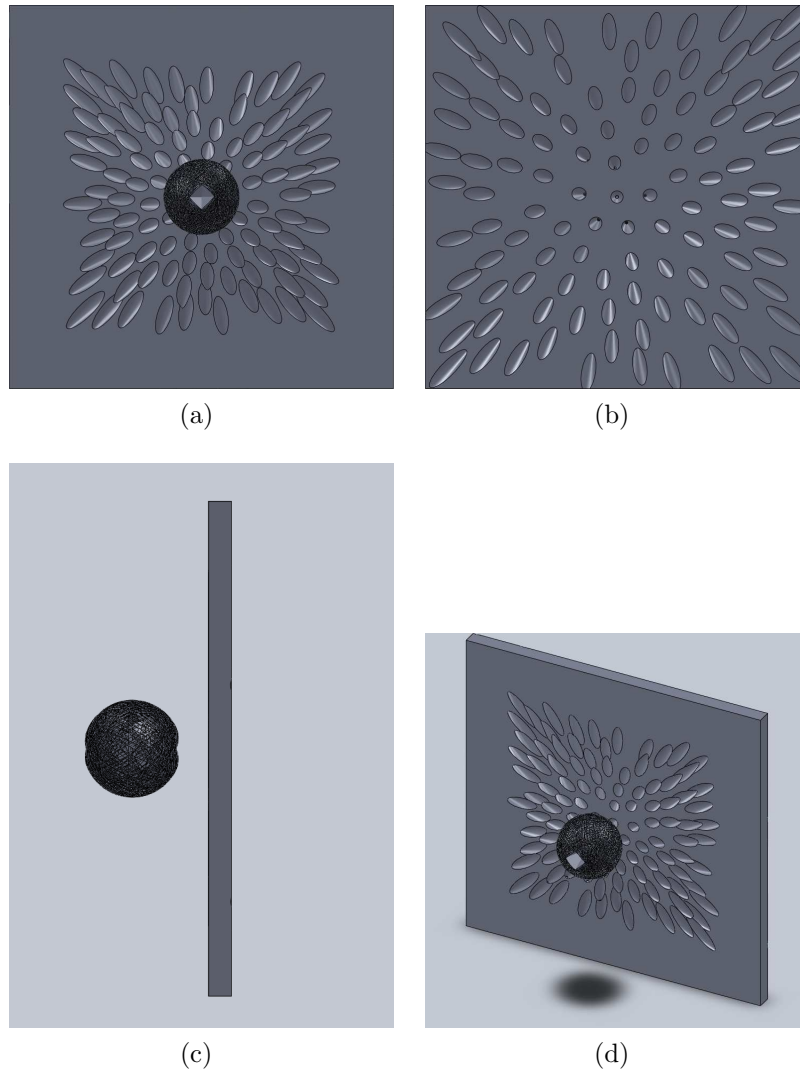


Figure 2: Several views of the collimator with the approximately spherical FOV visible. This was designed using SolidWorksTM and constructed using rapid-prototyping. It was then cast using a tungsten epoxy. The spherical object consists of the central slices of the FOV from which cones are projected to create the focused pinholes. The views are: (a) front view; (b) back view; (c) side view; (d) angled view.

2.2. System calibration

A discrete-to-discrete model of a SPECT system can be described by

$$\mathbf{g} = \mathbf{H}\mathbf{f}, \quad (3)$$

where the system matrix \mathbf{H} , maps an object, $\mathbf{f} = [f_1, \dots, f_N]^t$, into measured data $\mathbf{g} = [g_1, \dots, g_M]^t$. The object is decomposed as a set of N voxels, and the image as M data bins, therefore \mathbf{H} is a $M \times N$ matrix. The CCD data are binned to a 320×240 array of pixels, but not all of these pixels image the intensifier. The \mathbf{H} matrix is measured experimentally using a radioactive point source. The voxel function, f_n , is mimicked by stepping the point source through a 3D grid of measurement points in object space. For

each photon interaction in the scintillator there is a certain amount of light spread, and the light is detected as a cluster of pixels. A frame-parsing algorithm (Miller et al. 2009) extracts and processes each cluster. A centroid calculation is performed on the cluster to estimate the 2D interaction location. A projection image is stored for each voxel measurement, thus creating a system matrix that incorporates the imperfections, such as misalignments or non-uniformities, in the imaging system. This projection image is referred to as the point spread function (PSF). The mean system response is measured by recording many counts for each voxel position, and the object space is finely sampled with many voxel positions. This must be done for each system configuration (OP - PD combination). The response was measured on a $13 \times 13 \times 13$ cubic grid of points, with spacings of 2.5 mm, and interpolated to a grid of $97 \times 97 \times 97$ points, corresponding to cubic voxels with side-length of 0.3125 mm. This grid is greater than the common FOV, but it was measured to enable more accurate interpolation at the edges. Storing a projection image for each voxel of the interpolated grid would require > 250 GB of space for each system configuration. Although possible, it would be inefficient to store and read this data for every reconstruction. Instead, it is assumed that a point source projection through a pinhole has a 2D Gaussian distribution on the detector (Chen et al. 2005, Miller, Van Holen, Barrett & Furenlid 2012). A 2D Gaussian distribution is fitted to each PSF projection (section 2.3), and the coefficients of the fits are stored. Storing these coefficients requires < 0.5 GB for each system configuration.

2.3. Gaussian fitting and interpolation

The estimated interaction positions are binned to the nearest pixel, and the counts at each pixel are integrated. The integrated pinhole response function is represented as

$$f(x, y) = \frac{A}{2\pi\sigma_x\sigma_y\sqrt{1-\rho^2}} \times \exp\left\{-\frac{1}{2(1-\rho^2)}\left(\frac{(x-\bar{x})^2}{\sigma_x^2} + \frac{(y-\bar{y})^2}{\sigma_y^2} - \frac{2\rho(x-\bar{x})(y-\bar{y})}{\sigma_x\sigma_y}\right)\right\}. \quad (4)$$

The 2D Gaussians are fitted using a constrained non-linear optimization function in MatLabTM(fmincon), and six coefficients that characterize the Gaussian function are measured. The coefficients are the amplitude A , centroid location (\bar{x}, \bar{y}) , the x and y spread of the projection image (σ_x, σ_y) , and the correlation coefficient ρ .

The number of pinhole projections detected at each voxel location ranges from zero to forty-six. These pinholes must be identified, and associated with each other before interpolation can be performed. The algorithm is:

- (i) Select a base voxel, and identify the pinhole projections in the projected image as unique pinholes.
- (ii) Move to the nearest unprocessed voxel projection image.
- (iii) Extrapolate all currently known pinhole locations relating to this voxel position.
 - Each pinhole has a $13 \times 13 \times 13$ grid associated with it that stores the coefficients of that pinhole at each voxel location.
 - This grid is populated as the algorithm iterates through it.

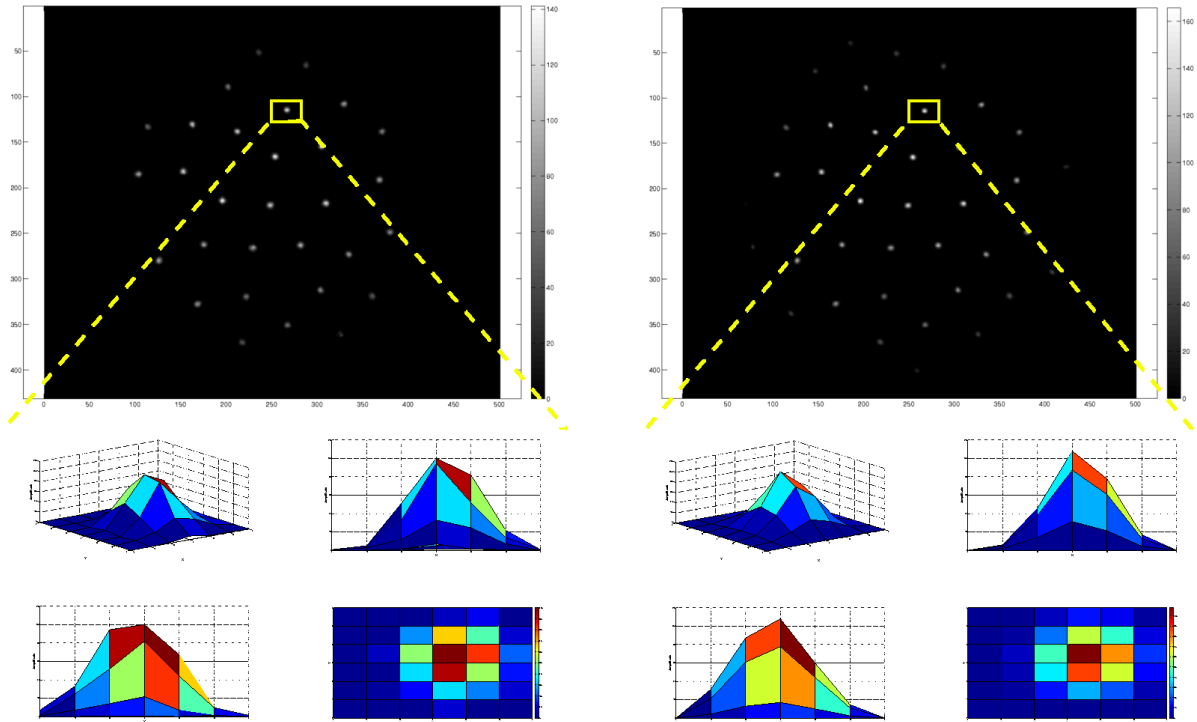


Figure 3: Raw PSF (left) and Gaussian fit (right) projections from a single voxel. Several views of a single projection distribution are shown below each image.

- Using the known data in this grid, estimate the position of a particular pinhole in a neighbouring voxel that has yet to be processed.
- (iv) Compare the predicted pinhole locations with the pinhole projections in this new image.
- If a pinhole projection is within the threshold distance of a predicted location it is identified as belonging to that pinhole, and the pinhole grid is updated.
 - If a pinhole projection is outside the threshold distance of every predicted location it means that this is a new pinhole that has not been identified yet. A new pinhole grid is created for this pinhole.
- (v) Repeat step (ii) until all voxel positions have been processed.

It is important to select a base image near the centre of the FOV with a large number of pinhole projections. The inter-voxel movements of the pinhole projections are smaller near the centre of the FOV than at the edge. This enables more precise extrapolation of pinhole projection locations at unprocessed voxel positions when the number of processed voxels is small. This algorithm is suitable for data in which the inter-voxel locations of the pinhole projections vary slightly. It was not possible to find a suitable threshold level that identified each pinhole accurately in data with much pinhole projection overlap. To overcome this problem, two low-magnification data sets were taken. The pinholes were identified, and associated between each voxel and between each data set. This information was then linearly extrapolated to predict the

locations of the pinhole projections in the high-magnification data. Due to the pinhole geometry, any pinhole projection visible in high-magnification data should be present in low-magnification data. The coefficients were then interpolated to a finer grid using cubic interpolation. Figure 4 shows the centroid positions of the Gaussian fits for all experimentally measured PSF locations.

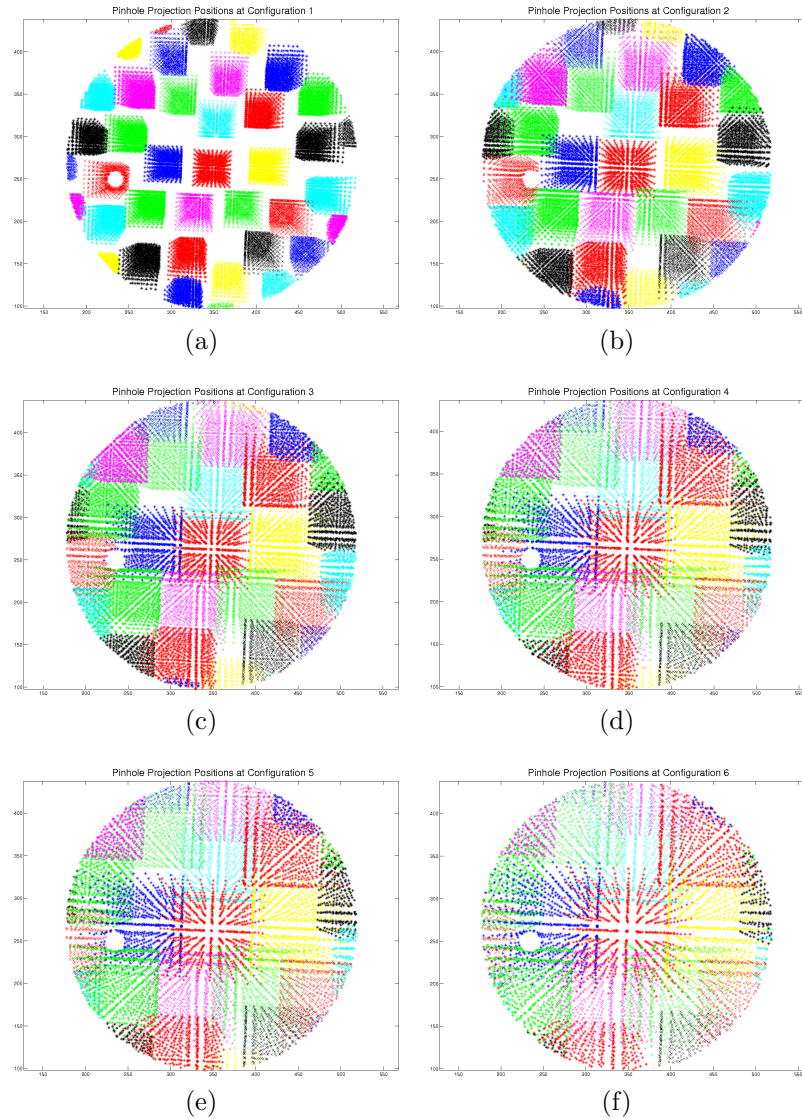


Figure 4: Centroid positions of the Gaussian coefficients fitted to the experimental pinhole projections for magnifications: (a) 0.4, (b) 0.8, (c) 1.1, (d) 1.5, (e) 1.6, (f) 2.0. The pinholes have been identified, and their detector positions are plotted. A range of colours is used to distinguish between the different pinhole projections. The PSF voxel grid can clearly be seen in the projections. The amount of projection overlap is proportional to the magnification. A small circular insensitive area of the intensifier can clearly be seen in the same location in all images.

2.4. Reconstruction

Image reconstruction was performed using maximum-likelihood expectation-maximization (MLEM). The elements of the system matrix were generated on-the-fly, using a GPU, from the interpolated Gaussian coefficients of the pinhole projections (Miller, Van Holen, Barrett & Furenlid 2012). The MLEM algorithm can be written as

$$\hat{f}_n^{(k+1)} = \frac{\hat{f}_n^{(k)}}{\sum_{m'=1}^M h_{m'n}} \sum_{m=1}^M \frac{g_m}{\sum_{n'=1}^N h_{mn'} \hat{f}_{n'}^{(k)}} h_{mn}, \quad (5)$$

where $\hat{f}_n^{(k)}$ is the estimated activity in voxel n after the k^{th} iteration, and h_{mn} is an element of \mathbf{H} that represents the probability that a photon emitted from voxel n is detected in detector element m . The activity in each of the voxels is estimated, and summing these activities along the axis perpendicular to the collimator face produces the 3D synthetic-collimator image. (Wilson et al. 2000).

2.5. Fourier crosstalk matrix

The Fourier crosstalk matrix fully describes all deterministic properties of the imaging system and provides a summary measure of resolution of the hardware alone, averaged over the FOV. A short description is provided in this work. A more detailed discussion can be found in (Barrett et al. 1995). From equation 3, the m_{th} detector measurement is given by

$$g_m = \int_S h_m(r) f(r) dr, \quad (6)$$

where S is the region defined by the support function $S(r)$, whose value is 1 if $r \in S$ and 0 otherwise. The object f can be represented by a Fourier series

$$f(r) = \sum_{k=-\infty}^{\infty} F_k \Phi_k(r), \quad (7)$$

where

$$\Phi_k(r) = e^{2\pi i \rho_k \cdot r} S(r), \quad (8)$$

is the k_{th} Fourier basis function. This vector index k spans an infinite set of integers (k_x, k_y, k_z) , and the wavevector ρ_k has the values

$$\rho_k = \frac{k}{L}, \quad (9)$$

where L is the width of the cubic region enclosing the space. This gives

$$g_m = \sum_{k=-\infty}^{\infty} F_k \Psi_{mk}, \quad (10)$$

where

$$\Psi_{mk} = \int_S h_m(r) e^{2\pi i \rho_k \cdot r} dr. \quad (11)$$

The detector sensitivity function, $h_m(r)$, describes the response of the m_{th} detector to a point source at r . An element of the Fourier crosstalk matrix is defined by

$$\beta_{kk'} = \sum_{m=1}^M \Psi_{mk}^* \Psi_{mk'}, \quad (12)$$

where M is the total number of detector elements. The diagonal element, β_{kk} , is the squared norm of the data when the object is a single Fourier-series component, and it quantifies how strongly a 3D spatial frequency contributes to the data. β_{kk} may therefore be interpreted as the square of the equivalent modulation transfer function (MTF_{eq}) of the system (Kim et al. 2006).

It is found that the width of the MTF_{eq}^2 , defined by its full-width half-maximum (FWHM), is a direct measure of the response of the system hardware to the Fourier components which fill the FOV. The resulting width is in units of spatial-frequency and is approximately Gaussian, so its Fourier transform is also approximately Gaussian. The FWHM of the resulting space-domain function along the three axes gives a measure of the 3D spatial resolution of the system, and may be used to compare tomographic systems. A Gaussian-distributed MTF_{eq} along the j axis can be written as

$$MTF_{eq}(j) = A_0 \exp\left(-\frac{j^2}{2\sigma^2}\right), \quad (13)$$

and its Fourier transform as

$$F\{MTF_{eq}(j)\} = A_0 \sqrt{2\pi\sigma^2} \exp(-2\pi^2\sigma^2\epsilon^2). \quad (14)$$

The FWHM of $MTF_{eq}(j)$ is $\sigma\sqrt{8\ln(2)}$, and that of $F\{MTF_{eq}(j)\}$ is $\sqrt{2\ln(2)}/\pi^2/\sigma$. The spatial resolution of the system along the j axis is

$$SpatialResolution = \frac{4\ln(2)}{\pi} \frac{1}{FWHM[MTF_{eq}(j)]}. \quad (15)$$

2.6. Phantom Imaging

As another measure of system performance, a hot-rod phantom with six sections containing capillaries with diameters 1.0, 1.2, 1.4, 1.6, 1.8 and 2.0 mm was imaged (figure 5). The distance between the rods in each section equals the diameter of the rods in that section. There is also a $10 \times 10 \times 2$ mm reservoir at the base of the phantom directly below the rods. The phantom was filled with ^{99m}Tc . The centre of the phantom was placed approximately at the centre of the FOV, with the rods oriented perpendicular to the detector, and the reservoir situated between the rods and the detector. Six images (figure 6) were taken at detector distances corresponding to magnifications of approximately 0.4, 0.8, 1.1, 1.5, 1.6 and 2.0. The images were formed using the same frame-parsing technique as outlined earlier. The acquisition time of each image was adjusted to account for isotope decay. The combined counts in the six images was $\sim 10^7$.

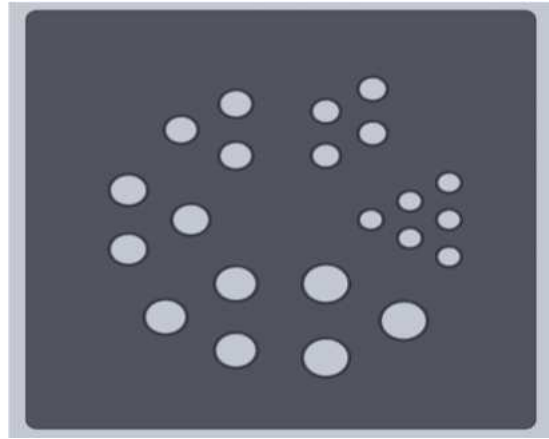


Figure 5: Image of the phantom used in this study. The diameters of the rods are 1.0, 1.2, 1.4, 1.6, 1.8, 2.0 mm, and the separation between the centres of the rods in each section is equal to twice the diameter of those rods. There is also a small $10 \times 10 \times 2$ mm reservoir at the base of the rods.

3. Results

3.1. Fourier crosstalk

The Fourier crosstalk matrix was used to estimate the average spatial resolution of the system. The plots of the MTF_{eq} , when all six system configurations are used, are shown in figure 7. The average spatial resolution, as each new system configuration was included in the calculation, is shown in figure 7d. The average spatial resolutions along the x and y axes (~ 2 mm) are very similar, as expected, and result in values close to that predicted for lateral resolution by traditional pinhole theory (Accorsi & Metzler 2005). As this is a limited-angle tomography system, it was expected that the spatial resolution in the z axis would be lower than in the x and y axes. It was found that the average spatial resolution along the z axis is approximately 8 mm. As noted earlier, these values represent the average resolution over the FOV without considering the reconstruction algorithm. By using a statistical iterative reconstruction algorithm, such as MLEM, it is possible to get better resolution at certain slices through the object than is estimated by the Fourier crosstalk matrix. Results of a hot-rod phantom imaging study are presented in the next section to confirm this.

3.2. Phantom experiment

The object, a hot-rod phantom with a small uniform reservoir, was reconstructed using 400 iterations of the MLEM algorithm, and post-smoothed with a Gaussian filter. The edge of the FOV has been removed due to excess build-up of estimated activity, as is common with MLEM. Every second slice of the reconstructed object within the FOV is shown in figure 8. Each image is a slice of the object at different distances from the collimator. The first slices (top left) are furthest from the collimator, and the last slices

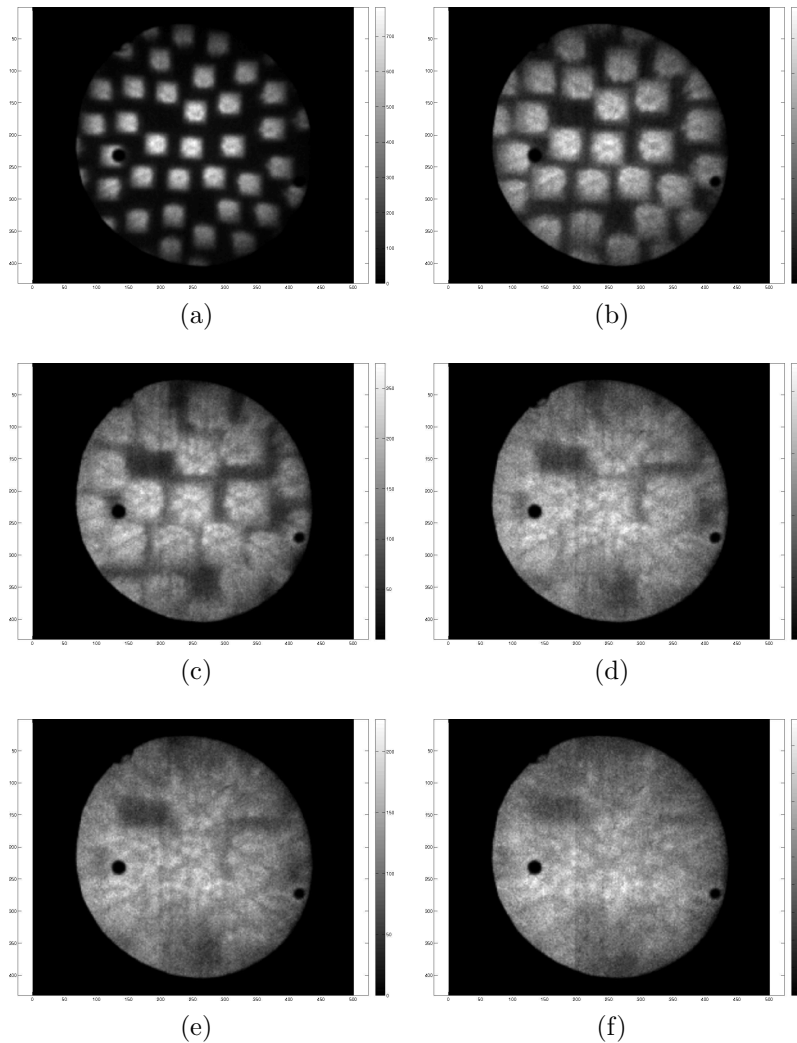


Figure 6: A hot-rod phantom is imaged at six geometric configurations corresponding to magnifications of: (a) 0.4, (b) 0.8, (c) 1.1, (d) 1.5, (e) 1.6 and (f) 2.0.

(lower right) are closer to the collimator. The rods were not entirely filled, although some activity is visible in the smaller rods in the slices furthest from the detector. This is due to these rods being used as injection sites for the ^{99m}Tc , and some activity may have attached to the walls of the rods. The 1.4 mm rods are resolved in several of the slices, although they are not clearly resolvable in the 3D synthetic-collimator image (figure 9). The 1.6 mm rods are the smallest diameter rods that are resolvable in the 3D synthetic-collimator image. It appears that one of the rods in the 1.6 mm set did not completely fill, and it is visible in only a small number of slices close to the collimator. This is the reason why it does not show a strong signal in the 3D synthetic-collimator image. The 1.8 mm and 2.0 mm rods are clearly resolvable in most of the slices throughout the FOV. The reservoir of activity at the base of the phantom is clearly seen, although uniform activity was not estimated accurately. This was expected as it is known that large uniform objects are difficult to reconstruct in limited-angle tomography.

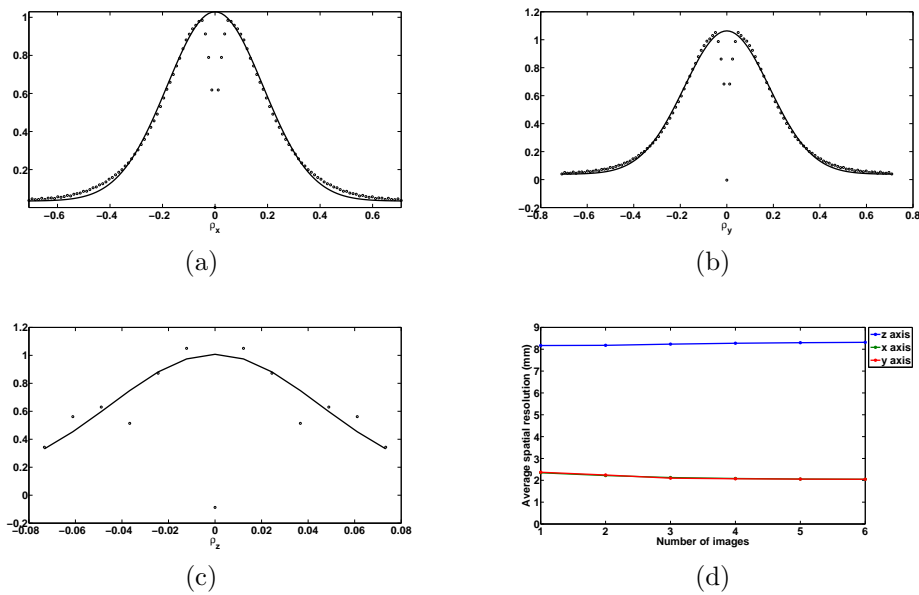


Figure 7: The normalized MTF_{eq} along the: (a) x axis, (b) y axis, (c) z axis. A Gaussian function (solid line) has been fitted to the MTF_{eq} data (dots). The average spatial resolution of the system is shown in (d), where the x axis denotes the number of system configurations used in the calculation. The average lateral resolution of the system improves as data from high-magnification configurations are included in the calculation.

4. Conclusion and discussion

An algorithm was developed to identify, and track, multiple pinhole projections throughout the FOV. This algorithm was used to accurately track forty-six pinhole projections on the detector over the entire FOV. The number of pinhole projections detected varied between the voxels, and extrapolation was performed to ensure accurate pinhole identification. Incorrect pinhole identification would lead to errors in the image reconstruction. 2D Gaussian distributions were fitted to the integrated pinhole projections for each voxel position. The coefficients of these fits were used to interpolate the system matrix. This interpolation was validated by successfully reconstructing a hot-rod phantom. The MLEM algorithm maximizes the probability of observing the detector data at each system configuration over all object densities. The large number of pinhole projections, the irregular pinhole pattern, and the varying magnifications, provide much information on an object distribution. Through the use of MLEM reconstruction the effect of multiplexing should be mitigated.

It is common to discuss peak performance of an imaging system rather than the average, however, the Fourier crosstalk matrix provides a figure of merit for the average spatial resolution of the system over the entire FOV. The crosstalk matrix may be used to optimize the system parameters when designing a system as it is calculated using the sensitivity function, and it is independent of the reconstruction algorithm.

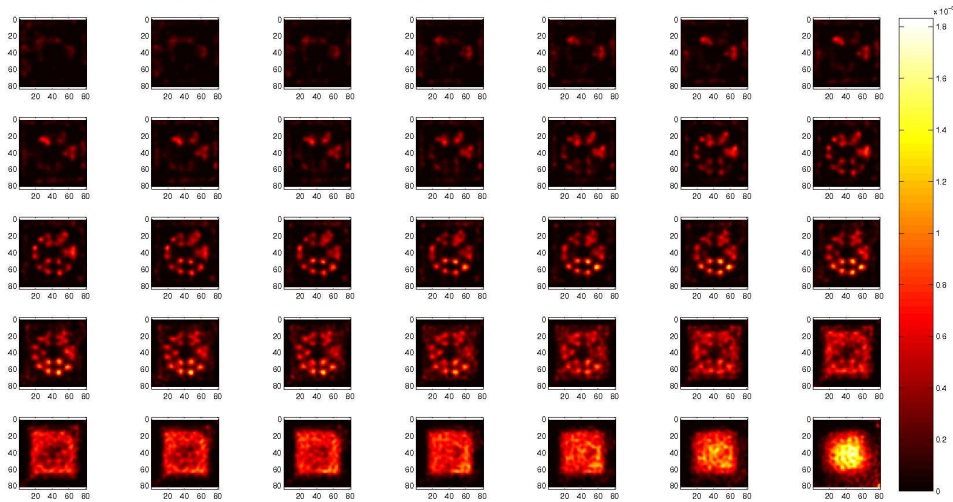


Figure 8: Every second slice (thickness = 0.3125 mm) through the z-axis of the object, after excluding the edges of the FOV. The first slice is furthest from the collimator, and the last slice is nearest to the collimator. The rods are partially filled, and so the rods are not visible in each slice. The injection sites, where some activity may have adhered to the walls of the rods, can be seen in the first few slices. The larger rods are becoming resolved at slice 13, and are resolvable until slice 26 where the activity from the small reservoir becomes dominant.

This study presented the design and construction of a SPECT imaging system that uses synthetic collimation to estimate the activity distribution within the FOV. Although it is a limited-angle tomography system, it is shown that some depth information can be estimated, likely due to the large number of pinhole projections acquired at low magnification. The 3D synthetic-collimator image was formed by summing the reconstructed voxels along the axis perpendicular to the collimator face. The number of pinhole projections detected decreases with increased magnification, as the solid angle subtended by the detector is reduced. A detector with a larger area will detect more pinhole projections at high magnification, and will allow the coefficients of the tube functions to be better estimated (Wilson et al. 2000). According to the findings of (Clarkson et al. 1998), the more data that is acquired, the better the estimates will be. In this work, all the data from six system configurations are used in the reconstruction. The pinholes were designed to have 1 mm diameters, although this may be larger in reality due to any problems filling the mold with the tungsten epoxy. Rods of 1.4 mm diameter can be distinguished in certain slices within the FOV, and 1.6 mm diameter rods are resolvable in the 3D synthetic-collimator image. The spatial resolution may be improved upon by reducing the diameter of the pinholes, increasing detector area, and by including data from higher-magnification system configurations.

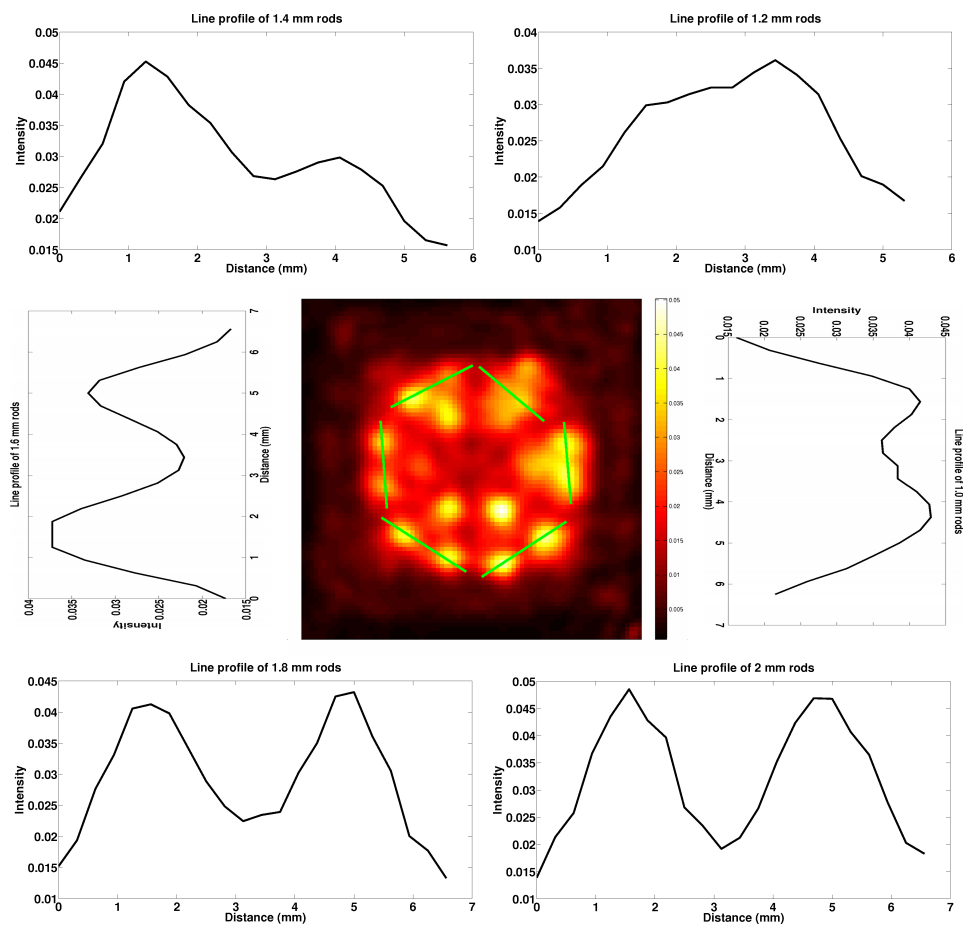


Figure 9: 3D synthetic-collimator image of the rod phantom. It is formed by summing the reconstructed voxels along the z axis, with z defined as the direction perpendicular to the collimator face. The line profiles for some of the rods are shown next to a green line highlighting the profile. The profiles were selected by joining the centroid of activity within each rod with the centroid of a neighbouring rod.

4.1. Acknowledgements

This work is supported by the United States National Institutes of Health under grant no. P41 EB002035.

References

- Accorsi R & Metzler S D 2005 *IEEE Trans Med Imaging*. **12**, 1637–46.
- Barrett H H, Denny J, Wagner R F & Myers K J 1995 *J. Opt. Soc. Am. A* **12**, 834–852.
- Barrett H H & Swindell W 1981 *Radiological Imaging: The theory of image formation, detection, and processing*. Academic Press.
- Cao Z, Bal G, Accorsi R & Acton P D 2005 *Phys. Med. Biol.* **50**(19), 4609.
- Chen Y C, Furenlid L R, Wilson D W & Barrett H H 2005 Springer chapter Calibration of Scintillation Cameras and Pinhole SPECT Imaging Systems., pp. 195–201.
- Cherry S 2004 *Phys. Med. Biol.* **49**, R13–R48.
- Clarkson E, Barrett H H & Wilson D W 1998 *SPIE* **3336**, 0277–786X.
- Dwyer R M, Ryan J, Havelin R J, Morris J C, Miller B W, Liu Z, Flavin R, O’Flatharta C, Foley M J, Barrett H H, Murphy J M, Barry F P, O’Brien T & Kerin M J 2011 *STEM CELLS* **29**(7), 1149–1157.
- Jaszczak R J, Li J, Wang H, Zalutsky M R & Coleman R E 1994 *Phys. Med. Biol.* **39**(3), 425.
- Kim H, Furenlid L, Crawford M J, Wilson D W, Barber H B, Peterson T, Hunter W C J, Liu Z, Woolfenden J M & Barrett H H 2006 *Med. Phys.* **33**(2), 465–474.
- Mahmood S T, Erlandsson K, Cullum L & Hutton B F 2010 *Phys. Med. Biol.* **55**(8), 2247.
- Meikle S R, Kench P, Kassiou M & Banati R B 2005 *Phys. Med. Biol.* **50**(22), R45.
- Miller B W, Barber H B, Barrett H H, Liu Z, Nagarkar V V & Furenlid L R 2012 in ‘SPIE Optical Engineering+ Applications’ International Society for Optics and Photonics pp. 85080F–85080F.
- Miller B W, Barber H B, Barrett H H, Wilson D W & Chen L 2006 in ‘Nuclear Science Symposium Conference Record, 2006. IEEE’ Vol. 6 IEEE pp. 3540–3545.
- Miller B W, Barber H B, Furenlid L R, Moore S K & Barrett H H 2009 *Proc SPIE*. **7450**(1996-756X), –.
- Miller B W, Barrett H H, Furenlid L R, Barber H B & Hunter R J 2008 *Nuclear Instruments and Methods in Physics Research, Section A: Accelerators, Spectrometers, Detectors and Associated Equipment* **591**(1), 272–275.
- Miller B W, Moore J W, Barrett H H, Fryé T, Adler S, Sery J & Furenlid L R 2011 *Nuclear Instruments and Methods in Physics Research Section A: Accelerators, Spectrometers, Detectors and Associated Equipment* .
- Miller B W, Van Holen R, Barrett H H & Furenlid L R 2012 *IEEE Transactions on Nuclear Science* **59** (5), 1990–1996.
- Min B J, Choi Y, Lee N Y, Lee K, Ahn Y B & Joung J 2009 *Nucl. Instrum. Methods Phys. Res.* **606**(3), 755.
- Peterson T E & Shokouhi S 2012 *J. Nucl. Med.* **53**, 841:844.
- Peterson T E, Shokouhi S, Furenlid L R & Wilson D W 2009 *IEEE Trans. Nucl. Sci.* **56**(3), 646.
- Shokouhi S, Metzler S D, Wilson D W & Peterson T E 2009 *Phys. Med. Biol.* **54**(2), 207.
- Vunckx K, Beque D, Defrise M & Nuyts J 2008 *IEEE Trans Med Imaging*. **27**(1), 36–46.
- Wilson D W, Barrett H H & Clarkson E W 2000 *IEEE Trans. Med. Imaging* **19**(5), 412.